Check for updates

ADVANCING EARTH AND SPACE SCIENCE

Geophysical Research Letters

RESEARCH LETTER
10.1029/2021GL096336

Key Points:

- I present a new multi-physics based model of the western United States
- The physical parameters are coupled through a newly developed variation of information constraint
- The models suggests that previous interpretations of the state of the lower crust are overly simplified and need to be revised

Supporting Information:

Supporting Information may be found in the online version of this article.

Correspondence to:

M. Moorkamp,
Max.Moorkamp@lmu.de

Citation:

Moorkamp, M. (2022). Deciphering the state of the lower crust and upper mantle with multi-physics inversion. *Geophysical Research Letters*, *49*, e2021GL096336. https://doi.org/10.1029/2021GL096336

Received 29 SEP 2021
Accepted 10 APR 2022

© 2022. The Authors.
This is an open access article under the terms of the Creative Commons Attribution License, which permits use, distribution and reproduction in any medium, provided the original work is properly cited.

Deciphering the State of the Lower Crust and Upper Mantle With Multi-Physics Inversion

Max Moorkamp[1]

[1]Department of Earth and Environmental Sciences, Ludwig-Maximilians-Universität, Munich, Germany

Abstract The composition of the lower crust is a key factor in understanding tectonic activity and deformation within the Earth. In particular, the presence or absence of melt or fluids has strong control on tectonic evolution. Multi-physics inversion results from the western United States indicate that tectonic inheritance plays a much stronger role in determining the location of melt in the lower crust than previously thought. Even in a currently active area such as the Yellowstone Hotspot, the results suggest that fluid dominated structures and fluid free regions are located directly next to each other. This is incompatible with the commonly used model of recent tectonic activity as a main controlling factor for the presence of fluids or melt. These results have global implications for how geophysical models are interpreted and how they can be related to geodynamic simulations.

Plain Language Summary The majority of knowledge about the state of the Earth comes from the interpretation of geophysical surveys. However, these surveys give results in terms of physical parameters, for example, electrical conductivity, and the relationship to phenomena of interest, for example, the amount of molten material or fluids at depth, is often ambiguous. I combine different geophysical measurements with a new method derived from medical imaging to reduce this ambiguity. Results from the western United States with this new method indicate that the way scientists so far inferred fluid content, for example, is overly simplified. It was thought that in geologically young and active regions fluids are wide-spread, while older and stable regions are virtually fluid free. Instead this study shows a more complex picture where geologic history determines the location of fluids in addition to current geologic activity. This will require a thorough revision of previous results not only in the United States but around the globe.

1. Introduction

The origin of low resistivity within the crust and upper mantle has been debated for more than five decades (Frost et al., 1989; Hyndman & Hyndman, 1968) since early electromagnetic observations revealed low resistivities at depths of 10–40 km within the Earth (Schmucker, 1964). Since then large scale array measurements and modern analyses based on two-dimensional and three-dimensional inversion of magnetotelluric (MT) data have shown that low resistivities at these depths are a widespread feature both in tectonically active (Meqbel et al., 2014; Wei et al., 2001) as well as stable continental regions (Moorkamp et al., 2019; Robertson et al., 2016) possibly with the exception of some Archean cratons (Jones & Ferguson, 2001). However, based on electrical resistivity alone it is not possible to infer the origin of these features as all potential causes currently under consideration: saline fluids, melt, graphite and sulphides can produce comparable resistivity anomalies (Jones, 1992). Therefore other geophysical observations and petrological considerations must be taken into consideration to determine the cause of low resistivity in the lower crust. For example, saline fluids and melt produce an observable low velocity anomaly in seismological models and qualitative comparisons between these methods have been used to infer fluids and melt in Tibet (Wei et al., 2001). Where such data are not available, general considerations based on regional heat flow and the tectonic setting have been used to argue the case for fluids (X. Li et al., 2020), melt (Heise et al., 2007), graphite (Robertson et al., 2016) or sulphides (Rao et al., 2007). This ancillary information has largely been used in a qualitative way and thus might not reflect the true complexity and heterogeneity within the Earth. In particular, such qualitative lines of reasoning are difficult to test quantitatively.

The north-western United States is a region of particular interest, as here active tectonics such as the subduction of the Juan de Fuca Plate, hotspot volcanism and active extension are directly adjacent to old lithosphere of the Wyoming craton and Colorado Plateau (Meqbel et al., 2014). Previous studies of the region have found wide-spread low-resistivity structures in the lower crust (Bedrosian & Feucht, 2014; Kelbert et al., 2012; Meqbel

et al., 2014). Given the aforementioned difficulties in identifying the cause of the low resistivity, these structures are attributed to reflect fluids and melts in the active western region and around Yellowstone and to graphite (Meqbel et al., 2014) or sulfides (Bedrosian & Feucht, 2014) in cratonic regions. Expanding on this idea, Liu and Hasterok (2016) construct a viscosity model along a profile from the Basin and Range to the Colorado Plateau where they associate low resistivity with low viscosity to perform simulations of lithospheric deformation and mantle flow. Their model successfully predicts various critical parameters including surface topography and highlights an avenue from static geophysical images to dynamic tectonic models, but critically hinges on the assumption that low resistivity in the crust corresponds to a zone of rheological weakness. While this is plausible for low resistivity caused by fluids, it might not be appropriate for a solid conductive phase (Selverstone, 2005).

Joint inversion of different geophysical data provides a quantitative approach to create multi-parameter models of the Earth (Moorkamp et al., 2016) and investigate the predictions made by the resulting model through sensitivity analyses. The presence of interconnected liquids such as saline fluids and melts results in low velocities, as mentioned above, but also in low bulk densities associated with the low resistivity structures due to the significantly lower density of the fluid components. In contrast, solid conductive phases such as graphite and sulphide have densities that are comparable to those of crustal rocks or even exceed them (Bellefleur et al., 2015). The combination of gravity measurements with MT data to investigate the lithosphere is particularly attractive as global geodetic models exist that combine satellite and terrestrial data and provide high-quality coverage for large parts of the globe (Pail et al., 2018).

2. Multi-Physics Inversion

I therefore combine long-period MT data from the north-western United States (de Groot-Hedlin et al., 2003-2004; Kelbert et al., 2011) with satellite gravity measurements (Pail et al., 2018) in order to investigate the causes of low-resistivity in this region. To focus on regional structure, the gravity data have been processed following the procedure of Szwillus et al. (2016) and described in more detail in Supporting Information S1. I use the joint inversion framework jif3D (Moorkamp et al., 2011) with a newly developed resistivity-density coupling criterion based on variation of information (VI) (Moorkamp, 2021). VI is an unsupervised machine-learning method which constructs, where possible, a one-to-one relationship of a-priori unspecified form between the properties under consideration (Haber & Holtzman Gazit, 2013; Mandolesi & Jones, 2014), in this case density and resistivity. Within the multi-physics inversion the misfit for the two data-sets under consideration as well as the VI constraint are minimized simultaneously, that is, the algorithm seeks a combined resistivity-density model that fits all observations and also shows maximum correspondence between the two physical properties.

Details about the multi-physics inversion software *jif3D* including the algorithms to solve the forward problem can be found in (Moorkamp et al., 2011). I therefore give only a brief summary of the main constituents and instead focus on the coupling through VI which has only been described briefly so far (Moorkamp, 2021). To construct the final combined density and resistivity model, the inversion solves a non-linear optimization problem with an objective function that consists of the data misfit for the MT and gravity observations, regularization terms for the conductivity and density models, respectively, and the VI based coupling term. It employs an iterative non-linear optimization method based on a limited memory quasi-Newton method (L-BFGS) (Avdeeva & Avdeev, 2006) with forward engines based on an integral equation approach for MT (Avdeev et al., 1997) and a massively parallel implementation for the gravity forward problem (Moorkamp et al., 2010). To ensure that conductivity and density remain within specified limits, the physical parameters are transformed to generalized parameters using the transform described in (Moorkamp et al., 2011) and the inverse problem is solved in this generalized parameter space. The two regularization terms are based on first-order forward differences to ensure smoothness of the model and reduce the influence of noisy measurements. I start the inversion with a large regularization parameter and successively relax the regularization until the inversion has converged to a data misfit comparable with the misfit for inversions based on each data set individually. More information about the evolution of the different terms of the objective function and a comparison with individual inversions can be found in in Supporting Information S1.

Variation of information is an information theoretical measure of the amount of information contained in variable $\boldsymbol{x}$ about another variable $\boldsymbol{y}$ and closely related to the concept of Mutual Information (Mandolesi & Jones, 2014). It is widely used in medical imaging (Pluim et al., 2003) and climate science (DelSole et al., 2013), but so far has

19448007, 2022, 9, Downloaded from https://agupubs.onlinelibrary.wiley.com/doi/10.1029/2021GL096336 by Cochrane Germany, Wiley Online Library on [10/10/2023]. See the Terms and Conditions (https://onlinelibrary.wiley.com/terms-and-conditions) on Wiley Online Library for rules of use; OA articles are governed by the applicable Creative Commons License

not been used in multi-physics imaging. To couple resistivity and density within the inversion framework, VI is minimized. This will result in models where, if possible, each density value corresponds to a unique resistivity value without prescribing a particular shape of that relationship. As it is provided as a term of the objective function in the inversion, this one-to-one relationship can be violated if mandated by the data to achieve a satisfactory fit.

To calculate the VI between conductivity and density I use a kernel density approach with a Gaussian kernel. However, the VI is not calculated on the quantities themselves, but on the generalized model parameters described above. This has the advantage that the input quantities are dimensionless and have comparable mean and variance. The first step in calculating VI is estimating the probability density distribution (pdd) for the joint parameters and the marginal distributions for each parameter. Denoting the pairs of transformed parameters in each model cell as (x_i, y_i) where $i = 1 \ldots M$ and M is the number of cells used to discretize the inverse problems, the pdd is approximated as

$$p(\xi_j, \eta_k) = \frac{1}{\sqrt{2\pi} M} \sum_{i=1}^{M} \exp\left(\frac{(x_i - \xi_j)^2 + (y_i - \eta_k)^2}{2\sigma^2}\right).$$

Here ξ_j and η_k are the discrete values at which we wish to approximate the pdd. For this study I use $N = 100$ evenly spaced values across the expected parameter range for each parameter and choose the standard deviation of the Gaussian, σ, as half the discretization width. From the joint pdd we can also calculate the marginal pdd's $p(\xi_j) = \sum_k p(\xi_j, \eta_k)$ and $p(\eta_k) = \sum_j p(\xi_j, \eta_k)$. In a second step we then calculate the Shannon Entropy $H(\mathbf{x}) = -\sum_i p(x_i) \log p(x_i)$ of the marginal and joint pdd's and finally retrieve the VI as

$$VI(\mathbf{x}, \mathbf{y}) = 2H(\mathbf{x}, \mathbf{y}) - H(\mathbf{x}) - H(\mathbf{y}).$$

The calculated VI is added to the inversion as a term in the objective function and thus minimized.

To use VI in an optimization context, we also need to calculate the partial derivatives with respect to the model parameters, that is, $\frac{\partial VI}{\partial \mathbf{x}}$ and $\frac{\partial VI}{\partial \mathbf{y}}$. This can be performed analytically by calculating the respective derivatives for the Gaussian kernel and applying the chain rule to account for the Entropy calculation. Using,

$$\frac{\partial p(\xi_j)}{\partial x_i} = -\frac{(x_i - \xi_j)}{\sqrt{2\pi} M \sigma^2} \sum_{k=1}^{N} \exp\left(\frac{(x_i - \xi_j)^2 + (y_i - \eta_k)^2}{2\sigma^2}\right)$$

and

$$\frac{\partial}{\partial x} x \log x = 1 + \log x$$

we have

$$\frac{\partial H(\mathbf{x})}{\partial x_i} = -\sum_{j=1}^{N} (1 + \log(p(\xi_j))) \frac{(x_i - \xi_j)}{\sqrt{2\pi} M \sigma^2} \sum_{k=1}^{N} \exp\left(\frac{(x_i - \xi_j)^2 + (y_i - \eta_k)^2}{2\sigma^2}\right),$$

and similarly for the other derivatives. Once the partial derivatives for entropy have been calculated, the derivative for VI can be calculated as a simple linear combination.

For the inversion an error floor of 2% of the maximum absolute value of impedance in each row of the impedance tensor for the MT data and 1–10 mGal for the gravity data based on the difference between a spherical approximation (Uieda et al., 2016) and a flat Earth approximation (Moorkamp et al., 2010) are assumed. With these uncertainty estimates, the inversion fits both datasets to RMS values of 1.9 (Gravity) and 1.6 (MT), respectively. These value are comparable to individual inversions of each data set and, for MT, the model of Meqbel et al. (2014). More information on the chosen errors, data fits and model assumptions can be found in in Supporting Information S1.

19448007, 2022, 9, Downloaded from https://agupubs.onlinelibrary.wiley.com/doi/10.1029/2021GL096336 by Cochrane Germany, Wiley Online Library on [10/10/2023]. See the Terms and Conditions (https://onlinelibrary.wiley.com/terms-and-conditions) on Wiley Online Library for rules of use; OA articles are governed by the applicable Creative Commons License

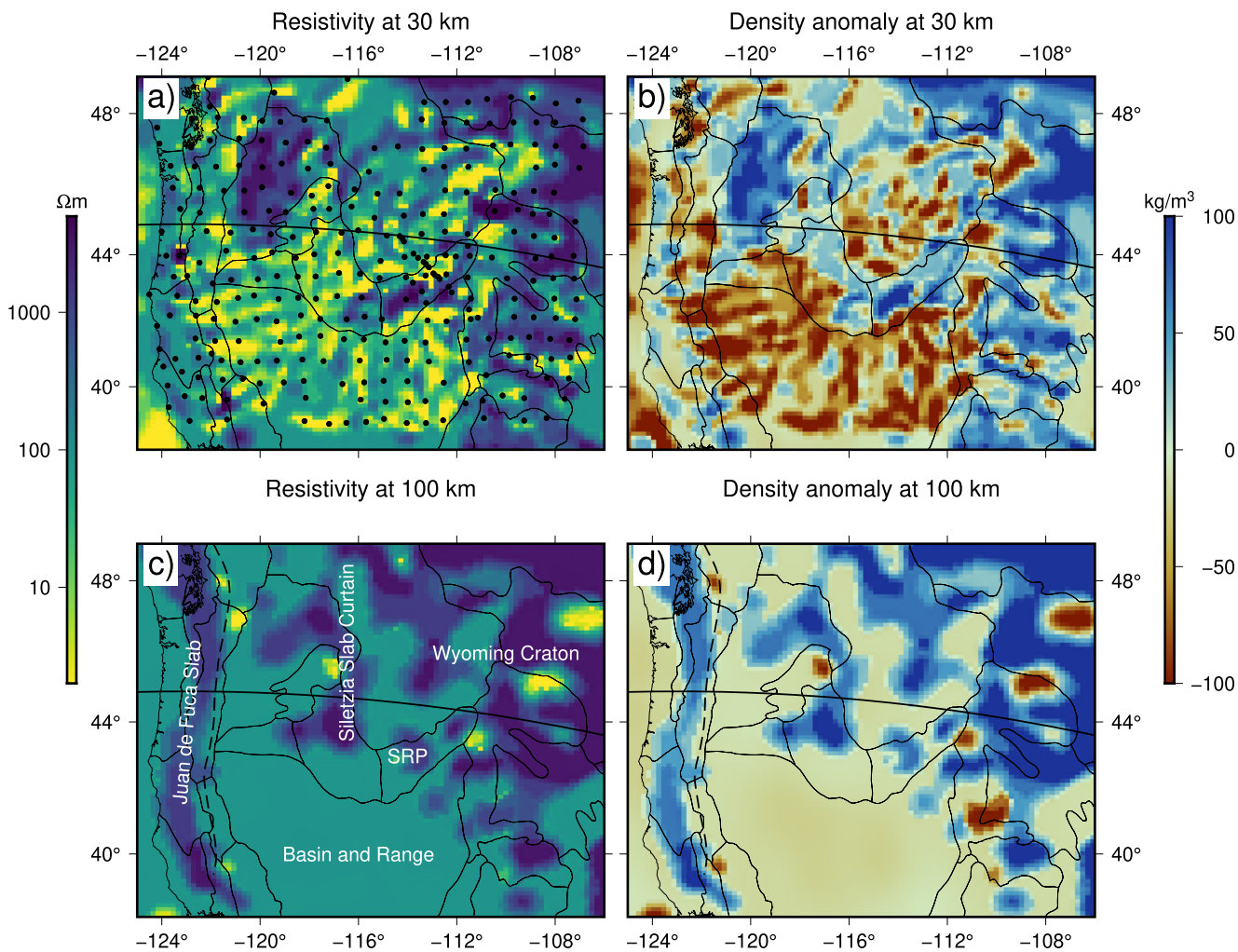

Figure 1. Horizontal slices through the integrated resistivity-density models at depths of 30 km (top row) and 100 km (bottom row). The locations of the magnetotelluric sites used for the inversion are shown in panel (a) The solid black line indicates the surface trace of the vertical profiles in Figure 2. The dashed line in panels (b and d) shows the boundary of the Juan de Fuca slab in the Slab2 model (Hayes et al., 2018). Also shown are the boundaries of the physiographic divisions (Fenneman & Johnson, 1946).

3. Integrated Model of the Western United States

Figure 1 shows horizontal slices through the resulting joint resistivity-density model at depths of 30 and 100 km which correspond to the base of the crust and the base of the lithosphere, respectively. The resistivity structure is generally consistent with previous models with enhanced definition of individual features (cf. Supporting Information S1). This is particularly evident at 100 km where the Juan de Fuca Slab and the Siletzia Slab Curtain (Schmandt & Humphreys, 2011) are imaged as sharp discrete features, but appear as broad resistive regions in models based on MT alone (Meqbel et al., 2014). Also note the remarkable coincidence between the eastern edge of the resistive feature associated with the Juan de Fuca Slab and the prediction made by the Slab2 model (Hayes et al., 2018) (dashed line in Figure 1). Within the mantle, several isolated conductive features can be observed which are consistent in location and shape with previously imaged features that have been interpreted as signatures of melt and slab-derived fluids (Meqbel et al., 2014). The mantle density model shows a strong correspondence to the resistivity model. Resistive features such as the active and remnant slabs are imaged as high density anomalies as expected and conversely low resistivity is associated with low density consistent with an interpretation of enhanced fluid content.

At 30 km depth, within the lower crust, the model shows low resistivities in large parts of the region, particularly in the tectonically active Basin and Range Region in the southern and western parts of the model. East of 110° W,

19448007, 2022, 9, Downloaded from https://agupubs.onlinelibrary.wiley.com/doi/10.1029/2021GL096336 by Cochrane Germany, Wiley Online Library on [10/10/2023]. See the Terms and Conditions (https://onlinelibrary.wiley.com/terms-and-conditions) on Wiley Online Library for rules of use; OA articles are governed by the applicable Creative Commons License

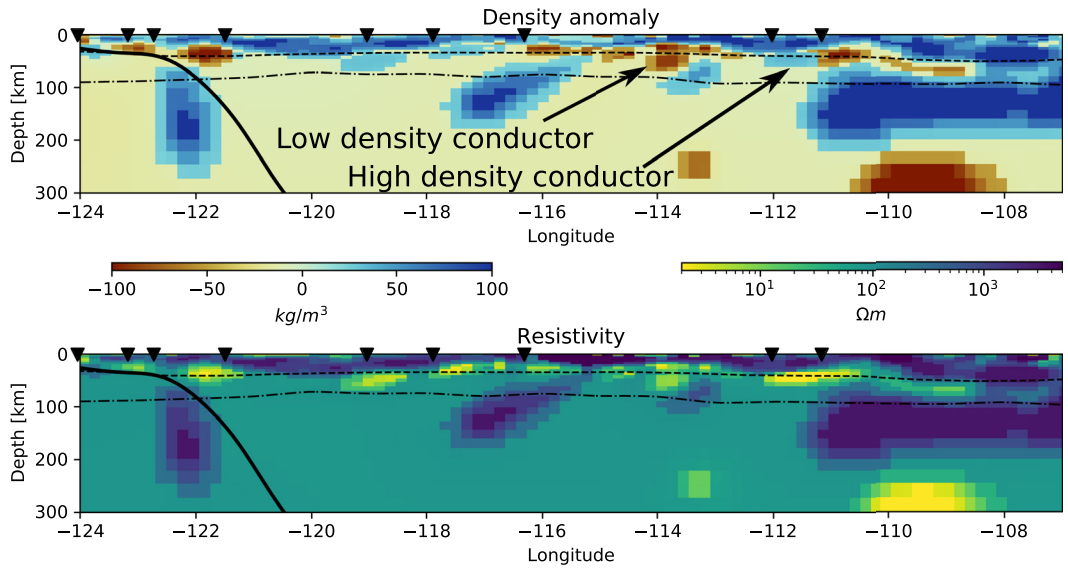

Figure 2. Vertical slices through the integrated model along the profile shown in Figure 1. Intersections with the physiographic divisions are marked with black inverted triangles. The thick black line shows the slab boundary from Slab2 (Hayes et al., 2018). The Moho (dashed line) (Szwillus et al., 2019) and the negative wave-speed disconinuity (NVD, dot dashed line) (Liu & Gao, 2018) are also shown.

toward the older shield regions, only isolated conductors are imaged. On the large scale, low resistivities correlate with negative density anomalies as discussed for the mantle above. However, in some areas we can identify deviations from this simple correlation. For example, the northern part of the Snake River Plain (SRP) shows significant regions where low resistivities correspond to high densities. To illustrate this further I show vertical slices through some of these anomalies in Figure 2.

The resistivity model (Figure 2) shows a series of low resistivity structures in the lower-most crust and uppermost mantle. The lateral boundaries of these structures generally coincide with boundaries between distinct physio-geographic regions. In all cases we can identify corresponding anomalies in the density model, however some of these show lower density than the background and others show higher densities than the background. Given the difficulty of gravity data to constrain the depth of causative features (e.g., Y. Li & Oldenburg, 1998), other models exist that can explain the gravity observations. However, under the coupling constraint and in combination with the MT data, the structural features and the relationship are robust under different inversion settings. Furthermore, it is important to note in this context that the VI constraint used to couple the two models aims at associating each resistivity value with a unique density value. Thus these different associations of high and low density with low resistivity values directly contradict the coupling constraint and need to be introduced in order to fit both datasets simultaneously.

4. Density-Resistivity Relationships

In order to investigate this observation further, the density-resistivity relationship for each cell in the joint model is plotted in Figure 3. The bulk of the estimates is located on a tight s-shaped curve. This shape has not been prescribed a-priori but evolves data-driven through the VI-constraint in the inversion. Outside the main spine of this relationship we observe some scatter related to heterogeneous near-surface structure but, more importantly, two leg-shaped features with near constant density and low resistivities between 0.5 and 20 Ωm. One of these (marked as high-density conductor in Figure 3) represents relatively dense and conductive material in the crust. It is close to neutrally buoyant and an increase in conductivity does not lead to a significant change in density. In contrast, the low density conductor (see Figure 3) at this depth shows a decrease in density with decreasing resistivity.

A possible explanation for the simultaneous decrease of resistivity and density for the low resistivity/low density structures is that the low resistivity is caused by highly conductive material with density significantly lower

19448007, 2022, 9, Downloaded from https://agupubs.onlinelibrary.wiley.com/doi/10.1029/2021GL096336 by Cochrane Germany, Wiley Online Library on [10/10/2023]. See the Terms and Conditions (https://onlinelibrary.wiley.com/terms-and-conditions) on Wiley Online Library for rules of use; OA articles are governed by the applicable Creative Commons License

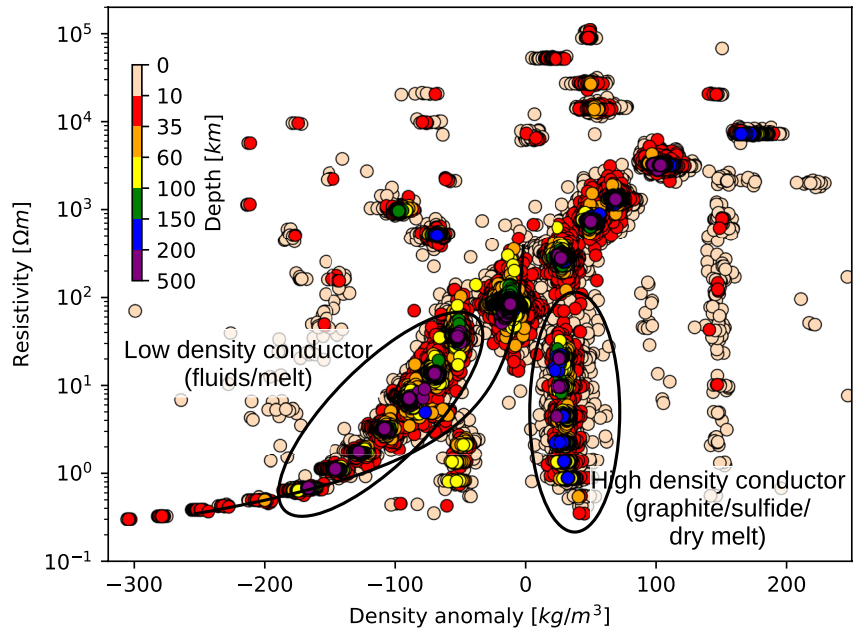

Figure 3. Resistivity versus density relationship extracted from the integrated inversion model. Each dot is colored by its corresponding depth. The black line shows the predicted density-resistivity relationship based on a fluid with a density contrast of −1,700 kg/m^3 and a conductivity of 50 S/m assuming a modified Archie's law (Glover et al., 2000).

than the host rock, for example, fluids or melt. Increasing the amount of conductive material then also has a strong impact on density. In fact, the observed relationship is broadly compatible with predictions of density and conductivity based on a modified Archie's law (Glover et al., 2000) (black line in Figure 3). For this calculation, I assume a density contrast of −1,700 kg/m^3 (based on an assumed host rock density of 2,800 kg/m^3 (Khatiwada & Keller, 2017) and a fluid density of 1,100 kg/m^3) and a conductivity of 50 S/m for the conductive phase as typically assumed for crustal fluids (Jones, 1992). These first-order calculations are not suitable for quantitative interpretation of fluid fraction, but demonstrate the consistency of the data derived estimates with petrophysical considerations.

For the low resistivity structures that are associated with a positive density anomaly, two explanations appear plausible: (a) The density of the host rock in this region is higher than in the surrounding regions and the conductive material still has a lower density than the host rock, possibly with a smaller density contrast. (b) The host rock density does not change very much, but the conductive material now has a density i.e., similar to the host rock or even exceeds it. In case of scenario (a), we expect to see a similar shape of this branch of the relationship to the low density conductor, that is, a decrease of density with decreasing resistivity, but starting from a different level. Instead there is a hint of a slight increase of density with decreasing resistivity. Trying to fit this part of the relationship with the modified Archie's law but a different density contrast shows significant deviations at the lowest resistivities even for small negative density contrasts for the conductive phase. Therefore scenario (b), a conductive phase with similar density to the host rock, is a more likely explanation. Graphite films or sulphide are two conductive materials often invoked in MT studies of the lithosphere (e.g., Rao et al., 2007) that are consistent with these inferences. Alternatively, dry basaltic melts can have densities that are very similar to that of solid rock (e.g., Colón et al., 2018; Iacovino & Till, 2019) and the change in density could be an expression of a transition from well hydrated melts to a dry melt composition. The idea of dry basaltic melt is also advocated by Kelbert et al. (2012) based on MT models for the SRP and surroundings. With the current level of analysis of the relationship it is not possible to distinguish between dry melt and graphite/sulphide. However, an interpretation of the results in terms of melt hydration raises the question why the models show abrupt lateral changes in density, as this would correspond to a sudden change in fluid content while melt fraction remains relatively constant. Furthermore, several of the high density conductors outside the SRP correspond to previously identified suture zones (Meqbel et al., 2014). Therefore, I prefer the interpretation of the high density conductors in terms of a solid phase, for example, graphite or sulphide, but cannot exclude a change of melt hydration.

19448007, 2022, 9, Downloaded from https://agupubs.onlinelibrary.wiley.com/doi/10.1029/2021GL096336 by Cochrane Germany, Wiley Online Library on [10/10/2023]. See the Terms and Conditions (https://onlinelibrary.wiley.com/terms-and-conditions) on Wiley Online Library for rules of use; OA articles are governed by the applicable Creative Commons License

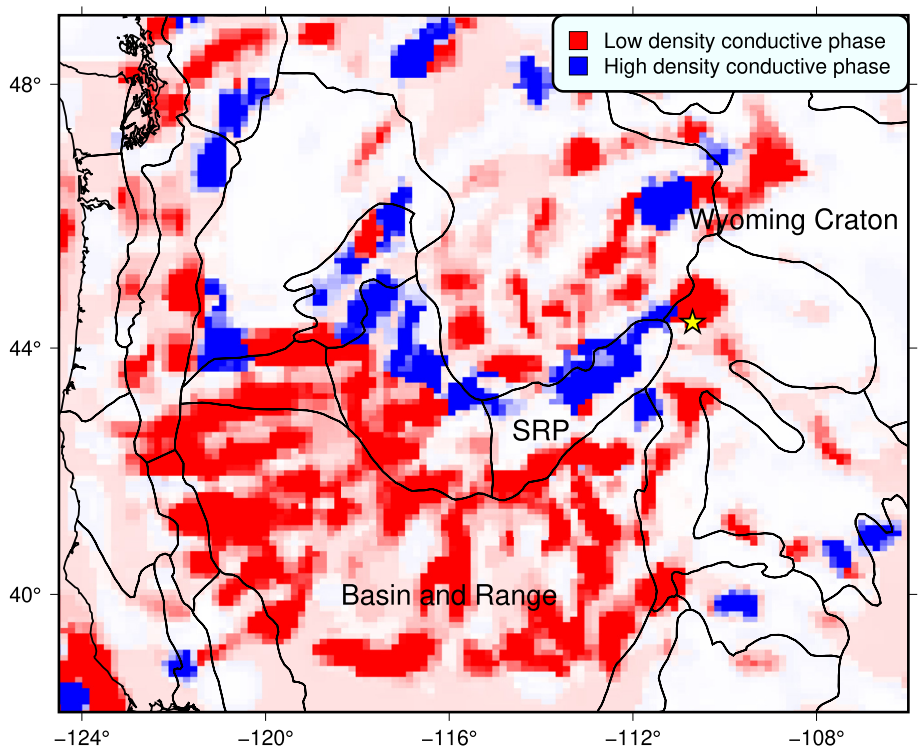

Figure 4. Conductive structures at depths between 28 and 39 km, corresponding to the lower crust and uppermost mantle, colored by density anomaly. Red indicates below average density at this depth indicating a liquid conductive phase, blue indicates neutral to above average density, associated with a solid conductive phase or dry melt. The location of the Yellowstone Hotspot is marked by a yellow star.

The locations of high-density (blue), and low density (red) conductive structures in the depth range between 28 and 39 km are summarized in Figure 4. Large parts of the region show conductive structures that are compatible with a fluid origin, for example, in the active Basin and Range province. However, fluid derived conductors are also identified along the assumed limits of the Wyoming Craton to the north east. Conversely, solid phase based conductive structures are found in the northern SRP and in close proximity to Yellowstone (marked by a yellow star in Figure 4). Although these solid phase conductors make up only a small volume of the observed conductive structures, the pattern is not random. There is a strong correlation with the northern boundary of the Snake Rive Plain and the transition from solid to fluid caused conductivity is strongly related to physio-geographic boundaries. A possible explanation is that this is the signature of a suture zone similar to those inferred further north (Meqbel et al., 2014).

It is difficult to attribute the inferred sulphide or graphite related low resistivity structures along the northern SRP to a single tectonic event due to the complex history of the region including subduction from the west, extension and the passage of the Yellowstone Hotspot (e.g., Khatiwada & Keller, 2017). To make it even more difficult to establish relationships between surface geology and deep structure, the SRP is largely covered in volcanics associated with the hotspot migration (e.g., Camp et al., 2015; Ellis et al., 2013). Despite these difficulties, multiple stages of deformation, exhumation of lower crustal material and zones of extensive shear have been reported along the edges of the SRP (e.g., Gray et al., 2020; Konstantinou et al., 2012; Tikoff et al., 2001). Most interestingly, Konstantinou and Miller (2015) postulate the existence of a long-lived major lithospheric boundary below the SRP similar to the Lewis and Clark Shear zone further north taking up deformation associated with low angle subduction of the Farallon Slab. The combination of carbon-influx through subduction and repeated deformation could have led to the development of extensive conductive graphite fabrics similar to those observed globally (e.g., Heinson et al., 2022). A detailed interpretation of the integrated results in terms of these processes requires more detailed analysis and high-resolution local data. However, these processes provide geological evidence that make the interpretation of the low resistivity/high density structures as caused by interconnected graphite plausible.

19448007, 2022, 9, Downloaded from https://agupubs.onlinelibrary.wiley.com/doi/10.1029/2021GL096336 by Cochrane Germany, Wiley Online Library on [10/10/2023]. See the Terms and Conditions (https://onlinelibrary.wiley.com/terms-and-conditions) on Wiley Online Library for rules of use; OA articles are governed by the applicable Creative Commons License

5. Implications for Global Interpretations

The complex pattern of structures retrieved by the joint inversion, indicates that the simple association of young and active tectonic areas with fluid caused conductivity and old regions with solid caused conductivity currently employed in the literature needs to be questioned. Instead it appears that changes in conductive phase are related to the location of tectonic boundaries. This suggests, that tectonic inheritance, that is, the control of older tectonic features on current processes (e.g., Audet & Bürgmann, 2011), can play a significant role in determining the origin of high conductivity in the lithosphere. A better understanding of these relationships is essential. For example, rheological modeling (Liu & Hasterok, 2016) was performed in the south-eastern part of the study area where the results are compatible with the assumed fluid derived conductivity. However, had this analysis been performed further to the north, this assumption would not hold. I have shown here how different causes of conductivity in the crust and mantle can be distinguished and these results require a new interpretation of the conductivity structure not only in the western United States but globally. For example, applying a similar multi-physics analysis to Tibet, where wide-spread fluids have been inferred based on electrical conductivity models (Wei et al., 2001), could potentially alter our understanding of the causes of low resistivity and result in different inferences on its geodynamics (Bai et al., 2010). Global application would mark an important step in understanding the composition of the lower crust and linking geophysical images to models of lithospheric dynamics. Beyond this, there is a wealth of additional information in the multi-physics models and the corresponding parameter relationships that I have not been able to discuss here. Thus these results are only the beginning of a new era of lithospheric imaging.

Data Availability Statement

The gravity data have been extracted from the global XGM2016 gravity model (Pail et al., 2018) which is accessible at http://doi.org/10.5880/icgem.2017.003. Grids for the study region can be obtained through the ICGEM calculation service http://icgem.gfz-potsdam.de/tom_longtime by selecting XGM2016 (model 161) and calculating the free-air anomaly (gravity_anomaly_cl). The magnetotelluric (MT) measurements have been acquired as part of the U.S. National Science Foundation's USArray MT program and de Groot-Hedlin et al. (2003-2004). They can be downloaded at https://ds.iris.edu/spud/emtf. The inversion codes used for this study can be obtained via subversion (https://subversion.apache.org) at svn checkout https://svn.code.sf.net/p/jif3d/jif3dsvn/trunk/jif3D jif3d. Processed data and model files can be found in Supporting Information S1 as well as https://doi.org/10.5281/zenodo.5799257.

Acknowledgments
This work was funded by the German Research Foundation, Deutsche Forschungsgemeinschaft, under grant MO 2265/4-1 and by the European Space Agency as part of the Support to Science Element 3D Earth. Alan G. Jones and Graham J. Hill provided helpful comments on an early version of the manuscript. Bernhard Weise provided the processed gravity data. Comments by the Editor Daoyuan Sun, Anna Kelbert and an anonymous reviewer are much appreciated and helped to improve the manuscript. Open access funding enabled and organized by Projekt DEAL.

References

Audet, P., & Bürgmann, R. (2011). Dominant role of tectonic inheritance in supercontinent cycles. *Nature Geoscience*, *4*(3), 184–187. https://doi.org/10.1038/ngeo1080

Avdeev, D. B., Kuvshinov, A. V., Pankratov, O. V., & Newman, G. A. (1997). High-performance three-dimensional electromagnetic modeling using modified Neumann series. Wide-band numerical solution and examples. *Journal of Geomagnetism and Geoelectricity*, *49*(11), 1519–1539. https://doi.org/10.5636/jgg.49.1519

Avdeeva, A., & Avdeev, D. (2006). A limited-memory quasi-Newton inversion for 1D magnetotellurics. *Geophysics*, *71*(5), G191–G196. https://doi.org/10.1190/1.2236381

Bai, D., Unsworth, M. J., Meju, M. A., Ma, X., Teng, J., Kong, X., et al. (2010). Crustal deformation of the eastern Tibetan plateau revealed by magnetotelluric imaging. *Nature Geoscience*, *3*(5), 358–362. https://doi.org/10.1038/ngeo830

Bedrosian, P. A., & Feucht, D. W. (2014). Structure and tectonics of the northwestern United States from EarthScope USArray magnetotelluric data. *Earth and Planetary Science Letters*, *402*, 275–289. https://doi.org/10.1016/j.epsl.2013.07.035

Bellefleur, G., Schetselaar, E., White, D., Miah, K., & Dueck, P. (2015). 3D seismic imaging of the Lalor volcanogenic massive sulphide deposit, Manitoba, Canada. *Geophysical Prospecting*, *63*(4), 813–832. https://doi.org/10.1111/1365-2478.12236

Camp, V. E., Pierce, K. L., & Morgan, L. A. (2015). Yellowstone plume trigger for Basin and Range extension, and coeval emplacement of the Nevada–Columbia Basin magmatic belt. *Geosphere*, *11*(2), 203–225. https://doi.org/10.1130/ges01051.1

Colón, D. P., Bindeman, I. N., & Gerya, T. (2018). Thermomechanical modeling of the formation of a multilevel, crustal-scale magmatic system by the Yellowstone plume. *Geophysical Research Letters*, *45*(9), 3873–3879. https://doi.org/10.1029/2018gl077090

de Groot-Hedlin, C., Constable, S., & Weitemeyer, K. (2003-2004). *Transfer functions for deep magnetotelluric sounding along the Yellowstone-Snake River hotspock track*. (retrieved from the IRIS database on Nov 01, 2018). https://doi.org/10.17611/DP/EMTF/YSRP/2004

DelSole, T., Kumar, A., & Jha, B. (2013). Potential seasonal predictability: Comparison between empirical and dynamical model estimates. *Geophysical Research Letters*, *40*(12), 3200–3206. https://doi.org/10.1002/grl.50581

Ellis, B., Wolff, J., Boroughs, S., Mark, D., Starkel, W., & Bonnichsen, B. (2013). Rhyolitic volcanism of the central Snake River plain: A review. *Bulletin of Volcanology*, *75*(8), 1–19. https://doi.org/10.1007/s00445-013-0745-y

Fenneman, N., & Johnson, D. (1946). *Physiographic divisions*.

Frost, B. R., Fyfe, W. S., Tazaki, K., & Chan, T. (1989). Grain-boundary graphite in rocks and implications for high electrical conductivity in the lower crust. *Nature*, *340*(6229), 134–136. https://doi.org/10.1038/340134a0

19448007, 2022, 9, Downloaded from https://agupubs.onlinelibrary.wiley.com/doi/10.1029/2021GL096336 by Cochrane Germany, Wiley Online Library on [10/10/2023]. See the Terms and Conditions (https://onlinelibrary.wiley.com/terms-and-conditions) on Wiley Online Library for rules of use; OA articles are governed by the applicable Creative Commons License

Glover, P. W., Hole, M. J., & Pous, J. (2000). A modified Archie's law for two conducting phases. *Earth and Planetary Science Letters*, *180*(3–4), 369–383. https://doi.org/10.1016/s0012-821x(00)00168-0

Gray, K. D., Isakson, V., Schwartz, D., & Vervoort, J. D. (2020). Orogenic link 41°N–46°N: Collisional mountain building and basin closure in the Cordillera of western North America. *Geosphere*, *16*(1), 136–181. https://doi.org/10.1130/ges02074.1

Haber, E., & Holtzman Gazit, M. (2013). Model fusion and joint inversion. *Surveys in Geophysics*, *34*(5), 675–695. https://doi.org/10.1007/s10712-013-9232-4

Hayes, G. P., Moore, G. L., Portner, D. E., Hearne, M., Flamme, H., Furtney, M., & Smoczyk, G. M. (2018). Slab2, a comprehensive subduction zone geometry model. *Science*, *362*(6410), 58–61. https://doi.org/10.1126/science.aat4723

Heinson, G., Kay, B., Loader, L., Robertson, K., & Thiel, S. (2022). A global magnetotelluric graphite type locality: Multi-decade, multi-scale studies of the Eyre Peninsula anomaly. *Gondwana Research*, *105*, 388–398. https://doi.org/10.1016/j.gr.2021.09.017

Heise, W., Bibby, H. M., Caldwell, T. G., Bannister, S. C., Ogawa, Y., Takakura, S., & Uchida, T. (2007). Melt distribution beneath a young continental rift: The Taupo Volcanic Zone, New Zealand. *Geophysical Research Letters*, *34*(14), L14313. https://doi.org/10.1029/2007gl029629

Hyndman, R., & Hyndman, D. (1968). Water saturation and high electrical conductivity in the lower continental crust. *Earth and Planetary Science Letters*, *4*(6), 427–432. https://doi.org/10.1016/0012-821x(68)90017-4

Iacovino, K., & Till, C. B. (2019). Densityx: A program for calculating the densities of magmatic liquids up to 1,627 c and 30 kbar. *Volcanica*, *2*(1), 1–10. https://doi.org/10.30909/vol.02.01.0110

Jones, A. G. (1992). Electrical conductivity of the continental lower crust. *Continental lower crust*, 81–143.

Jones, A. G., & Ferguson, I. J. (2001). The electric moho. *Nature*, *409*(6818), 331–333. https://doi.org/10.1038/35053053

Kelbert, A., Egbert, G., & deGroot Hedlin, C. (2012). Crust and upper mantle electrical conductivity beneath the Yellowstone Hotspot Track. *Geology*, *40*(5), 447–450. https://doi.org/10.1130/g32655.1

Kelbert, A., Egbert, G., & Schultz, A. (2011). *Iris dmc data services products: EMTF, the magnetotelluric transfer functions*. https://doi.org/10.17611/DP/EMTF.1. (retrieved from the IRIS database on Mar 20, 2021).

Khatiwada, M., & Keller, G. R. (2017). A crustal-scale integrated geophysical and tectonic study of the Snake River Plain region, northwestern USA. *International Geology Review*, *59*(15), 1929–1943. https://doi.org/10.1080/00206814.2017.1303647

Konstantinou, A., & Miller, E. (2015). Evidence for a long-lived accommodation/transfer zone beneath the Snake River plain: A possible influence on Neogene magmatism? *Tectonics*, *34*(12), 2387–2398. https://doi.org/10.1002/2015tc003863

Konstantinou, A., Strickland, A., Miller, E. L., & Wooden, J. P. (2012). Multistage Cenozoic extension of the Albion–Raft River–Grouse Creek metamorphic core complex: Geochronologic and stratigraphic constraints. *Geosphere*, *8*(6), 1429–1466. https://doi.org/10.1130/ges00778.1

Li, X., Ma, X., Chen, Y., Xue, S., Varentsov, I. M., & Bai, D. (2020). A plume-modified lithospheric barrier to the southeastward flow of partially molten Tibetan crust inferred from magnetotelluric data. *Earth and Planetary Science Letters*, *548*, 116493. https://doi.org/10.1016/j.epsl.2020.116493

Li, Y., & Oldenburg, D. W. (1998). 3-D inversion of gravity data. *Geophysics*, *63*(1), 109–119. https://doi.org/10.1190/1.1444302

Liu, L., & Gao, S. S. (2018). Lithospheric layering beneath the contiguous United States constrained by S-to-P receiver functions. *Earth and Planetary Science Letters*, *495*, 79–86. https://doi.org/10.1016/j.epsl.2018.05.012

Liu, L., & Hasterok, D. (2016). High-resolution lithosphere viscosity and dynamics revealed by magnetotelluric imaging. *Science*, *353*(6307), 1515–1519. https://doi.org/10.1126/science.aaf6542

Mandolesi, E., & Jones, A. G. (2014). Magnetotelluric inversion based on mutual information. *Geophysical Journal International*, *199*(1), 242–252. https://doi.org/10.1093/gji/ggu258

Meqbel, N. M., Egbert, G. D., Wannamaker, P. E., Kelbert, A., & Schultz, A. (2014). Deep electrical resistivity structure of the northwestern US derived from 3-d inversion of USArray magnetotelluric data. *Earth and Planetary Science Letters*, *402*, 290–304. https://doi.org/10.1016/j.epsl.2013.12.026

Moorkamp, M. (2021). Joint inversion of gravity and magnetotelluric data from the Ernest-Henry IOCG deposit with a variation of information constraint. In *First international meeting for applied geoscience & energy* (pp. 1711–1715). https://doi.org/10.1190/segam2021-3582000.1

Moorkamp, M., Fishwick, S., Walker, R. J., & Jones, A. G. (2019). Geophysical evidence for crustal and mantle weak zones controlling intraplate seismicity–the 2017 Botswana earthquake sequence. *Earth and Planetary Science Letters*, *506*, 175–183. https://doi.org/10.1016/j.epsl.2018.10.048

Moorkamp, M., Heincke, B., Jegen, M., Roberts, A. W., & Hobbs, R. W. (2011). A framework for 3-D joint inversion of MT, gravity and seismic refraction data. *Geophysical Journal International*, *184*(1), 477–493. https://doi.org/10.1111/j.1365-246X.2010.04856.x

Moorkamp, M., Jegen, M., Roberts, A., & Hobbs, R. (2010). Massively parallel forward modeling of scalar and tensor gravimetry data. *Computers & Geosciences*, *36*(5), 680–686. https://doi.org/10.1016/j.cageo.2009.09.018

Moorkamp, M., Lelièvre, P. G., Linde, N., & Khan, A. (Eds.). (2016). *Integrated imaging of the Earth*, (Vol. 218). John Wiley & Sons, Inc. *Geophysical Monograph Series*. https://doi.org/10.1002/9781118929063

Pail, R., Fecher, T., Barnes, D., Factor, J., Holmes, S., Gruber, T., & Zingerle, P. (2018). Short note: The experimental geopotential model XGM2016. *Journal of Geodesy*, *92*(4), 443–451. https://doi.org/10.1007/s00190-017-1070-6

Pluim, J., Maintz, J., & Viergever, M. (2003). Mutual-information-based registration of medical images: A survey. *IEEE Transactions on Medical Imaging*, *22*(8), 986–1004. https://doi.org/10.1109/tmi.2003.815867

Rao, C. K., Jones, A. G., & Moorkamp, M. (2007). The geometry of the Iapetus Suture Zone in central Ireland deduced from a magnetotelluric study. *Physics of the Earth and Planetary Interiors*, *161*(1–2), 134–141. https://doi.org/10.1016/j.pepi.2007.01.008

Robertson, K., Heinson, G., & Thiel, S. (2016). Lithospheric reworking at the Proterozoic–Phanerozoic transition of Australia imaged using AusLAMP magnetotelluric data. *Earth and Planetary Science Letters*, *452*, 27–35. https://doi.org/10.1016/j.epsl.2016.07.036

Schmandt, B., & Humphreys, E. (2011). Seismically imaged relict slab from the 55 Ma Siletzia accretion to the northwest United States. *Geology*, *39*(2), 175–178. https://doi.org/10.1130/g31558.1

Schmucker, U. (1964). Anomalies of geomagnetic variations in the southwestern United States. *Journal of Geomagnetism and Geoelectricity*, *15*(4), 193–221. https://doi.org/10.5636/jgg.15.193

Selverstone, J. (2005). Preferential embrittlement of graphitic schists during extensional unroofing in the Alps: The effect of fluid composition on rheology in low-permeability rocks. *Journal of Metamorphic Geology*, *23*(6), 461–470. https://doi.org/10.1111/j.1525-1314.2005.00583.x

Szwillus, W., Afonso, J. C., Ebbing, J., & Mooney, W. D. (2019). Global crustal thickness and velocity structure from geostatistical analysis of seismic data. *Journal of Geophysical Research: Solid Earth*, *124*(2), 1626–1652. https://doi.org/10.1029/2018jb016593

Szwillus, W., Ebbing, J., & Holzrichter, N. (2016). Importance of far-field topographic and isostatic corrections for regional density modelling. *Geophysical Journal International*, *207*(1), 274–287. https://doi.org/10.1093/gji/ggw270

19448007, 2022, 9, Downloaded from https://agupubs.onlinelibrary.wiley.com/doi/10.1029/2021GL096336 by Cochrane Germany, Wiley Online Library on [10/10/2023]. See the Terms and Conditions (https://onlinelibrary.wiley.com/terms-and-conditions) on Wiley Online Library for rules of use; OA articles are governed by the applicable Creative Commons License

Tikoff, B., Kelso, P., Manduca, C., Markley, M., & Gillaspy, J. (2001). Lithospheric and crustal reactivation of an ancient plate boundary: The assembly and disassembly of the Salmon River suture zone, Idaho, USA. *Geological Society, London, Special Publications*, *186*(1), 213–231. https://doi.org/10.1144/gsl.sp.2001.186.01.13

Uieda, L., Barbosa, V. C., & Braitenberg, C. (2016). Tesseroids: Forward-modeling gravitational fields in spherical coordinates. *Geophysics*, *81*(5), F41–F48. https://doi.org/10.1190/geo2015-0204.1

Wei, W., Unsworth, M., Jones, A., Booker, J., Tan, H., Nelson, D., et al. (2001). Detection of widespread fluids in the Tibetan crust by magnetotelluric studies. *Science*, *292*(5517), 716–719. https://doi.org/10.1126/science.1010580

References From the Supporting Information

Avdeeva, A., Moorkamp, M., Avdeev, D., Jegen, M., & Miensopust, M. (2015). Three-dimensional inversion of magnetotelluric impedance tensor data and full distortion matrix. *Geophysical Journal International*, *202*(1), 464–481. https://doi.org/10.1093/gji/ggv144

Moorkamp, M., Avdeeva, A., Basokur, A. T., & Erdogan, E. (2020). Inverting magnetotelluric data with distortion correction—Stability, uniqueness and trade-off with model structure. *Geophysical Journal International*, *222*(3), 1620–1638. https://doi.org/10.1093/gji/ggaa278

19448007, 2022, 9, Downloaded from https://agupubs.onlinelibrary.wiley.com/doi/10.1029/2021GL096336 by Cochrane Germany, Wiley Online Library on [10/10/2023]. See the Terms and Conditions (https://onlinelibrary.wiley.com/terms-and-conditions) on Wiley Online Library for rules of use; OA articles are governed by the applicable Creative Commons License